PAPER

Check for updates

Degradation of formaldehyde aqueous solution by Bi based catalyst and its activity evaluation

Runquan Wang, [ID] [ab] Yuerong Zhang,[ab] Wanping Chen,[ab] Yuan Tian,[ab] Kai Song,[ab] Jiaxian Li,[ab] Guoying Wang[ab] and Gaofeng Shi*[ab]

Bi based catalysts have attracted continuous attention from the scientific community because of their excellent photochemical properties and wide application in photocatalytic treatment of environmental pollution. A series of Bi based catalysts with good crystallinity and high purity were prepared by calcination and hydrothermal synthesis. In the application of degrading formaldehyde aqueous solution in a mercury lamp and xenon lamp atmosphere, it was found that $BiVO_4$ and Bi_2WO_6 showed excellent photochemical properties under ultraviolet and visible light. The tests of PL, UV-Vis and EIS confirmed their high activity. In the calculation based on density functional theory (DFT), through the analysis of the energy band structure, density of states (DOS) and partial wave density of states (PDOS), it is found that the d orbital of V and W elements has a great influence on the position and size of the energy band of the catalyst, which makes it have high activity and excellent electrochemical properties.

1. Introduction

Bismuth as a non noble metal, and has a wide range of sources, low price and high electron transfer rate.[1,2] It has become an effective alternative metal element for noble metal catalysts.[3] Bi based catalysts have many advantages over other metal catalysts.[4,5] Firstly, when Bi participates in the formation of oxides, it often exists in the form of Bi^{3+}. Its valence band is not composed of a single atomic orbital, but is formed by the hybridization of the 2p orbital of the O atom and the 6s orbital of the Bi atom.[6] The lone pair electron distortion on the 6s orbital of the Bi atom makes the O 2p and Bi 6s orbitals overlap obviously,[7,8] which is convenient for charge migration.[9] It also changes the original band structure of the compound. At the same time, Bi series photocatalysts have been widely studied because of the special structure of alternating layers and more suitable band edges due to the surface plasmon resonance (SPR)[10] effect, and can be used as cocatalysts to promote charge separation and improve the efficiency of photocatalysts.[11] For example, Li *et al.*[12] mentioned that Bi modification can improve the conversion efficiency of Co and g-C_3N_4 catalysts. Therefore, based on the particularity of Bi based photocatalyst materials,[13] it is of certain value and significance to study the catalytic activity of bismuth compounds in photocatalysis.[14,15]

Different Bi based metal catalysts, such as Bi_2O_3, $BiVO_4$, Bi_2WO_6, BiOI, BiOBr and Bi_2S_3, were prepared by calcination and hydrothermal synthesis,[16] and their structure, morphology and photoelectrochemical properties were analyzed.[17] It was applied to the study of photocatalytic degradation of formaldehyde aqueous solution; the mechanism of photocatalytic degradation of formaldehyde aqueous solution[18] was analyzed by studying the catalytic activities of different Bi based catalysts in the range of visible light and ultraviolet light.[19,20] At the same time, based on the density functional theory (DFT),[21,22] the energy band, density of states (DOS) and partial wave density of states (PDOS)[23] of the catalyst material are calculated on the platform of Mede A. The catalytic activity of Bi based catalyst is evaluated through theoretical calculation, and the results are mutually verified[24] and analyzed with the experimental results.

2. Experimental section

2.1 Materials and reagents

Bismuth nitrate pentahydrate, nitric acid (65–68%, wt), sodium hydroxide, anhydrous ethanol, citric acid, sodium tungstate, ethylene glycol monomethyl ether, potassium iodide, potassium bromide, thioacetamide, formaldehyde aqueous solution (36–38%, wt), potassium bromate, *p*-benzoquinone, ammonium oxalate, diphenylamine, acetopropione, glacial acetic acid, ammonium acetate. The above drugs are analytical pure.

Preparation of Bi_2O_3: put 5.00 g $Bi(NO_3)_3 \cdot 5H_2O$ crystal in muffle furnace and calcine at 450 °C for 4 h to obtain pure Bi_2O_3 crystal.

Preparation of $BiVO_4$ solution A: dissolve 2 mmol of $Bi(NO_3)_3 \cdot 5H_2O$ crystal in 13% nitric acid solution; liquid B: put

[a]School of Petrochemical Technology, Lanzhou University of Technology, Lanzhou, 730100, China. E-mail: gaofengshi_lzh@163.com

[b]Key Laboratory of Low Carbon Energy and Chemical Engineering of Gansu Province, Lanzhou, 730100, China

2 mmol Na$_3$VO$_4$·12H$_2$O crystal into 10.00 mL deionized water and stir. Add liquid a to liquid B, adjust the pH of the solution to neutral with (NaOH/HNO$_3$), stir for 30 min, add it to the hydrothermal synthesis kettle lined with polytetrafluoroethylene, and conduct hydrothermal synthesis at 120 °C for 12 h. First wash the synthesized solid with deionized water to neutral, then wash it with water-free ethanol for 3 times, and dry it in an oven at 100 °C for 8 h to obtain BiVO$_4$ crystal.[25]

Preparation of Bi$_2$WO$_6$: place 5 mmol Bi (NO$_3$)$_3$·5H$_2$O crystal and 2.00 g citric acid in 30.00 mL deionized water, stir for a certain time, add 2.5 mmol Na$_2$WO$_4$·2H$_2$O crystal, stir for a certain time, place it in a hydrothermal synthesis kettle, react at 180 °C for 20 h, wash the obtained solid with deionized water and anhydrous ethanol for 3 times respectively, and dry at 80 °C for 12 h to obtain Bi$_2$WO$_6$ crystal.[26]

Preparation of BiOI: mix ethylene glycol monomethyl ether with water according to 1 : 1 (volume ratio); solution A: add 2.5 mmol Bi (NO$_3$)$_3$·5H$_2$O crystal into 25.00 mL mixed solution and stir; solution B: dissolve 2.5 mmol KI in 25.00 mL mixed solution and stir; add liquid B drop by drop into liquid a, stir it for a certain time, put it in a hydrothermal synthesis kettle, synthesize it at 160 °C for 6 h, use deionized water centrifugal lotion for 3 times, put it in an oven and dry it at 80 °C for 12 h to obtain BiOI crystal[27](replace KI with KBr or thioacetamide to obtain BiOBr[28,29] and Bi$_2$S$_3$ (ref. 30) crystals respectively).

2.2 Characterization of materials

The materials were characterized by scanning electron microscopy (SEM), Fourier infrared spectroscopy (FT-IR), X-ray diffraction (XRD), Brunauer–Emmett–Teller (BET), X-ray photoelectron spectroscopy (XPS), photoluminescence spectroscopy (PL), Raman spectroscopy, UV-Vis diffuse reflectance spectroscopy and electrochemical analysis.

2.3 Photocatalytic degradation of formaldehyde aqueous solution

The photocatalytic degradation experiment is to prepare 0.5 mg mL^{-1} aqueous formaldehyde solution as the reaction solution, and the amount of catalyst is 2.5 g L^{-1}, which is radiated under mercury lamp and xenon lamp respectively.[31] In the process of degradation, take out 0.50 mL of reaction solution sample according to the predetermined time gradient. After that, transfer it into the liquid sampling bottle and quantitatively analyze the formaldehyde in the reaction solution by acetylacetone ultraviolet spectrophotometer. The specific operations are as follows: accurately transfer 0.24 mL of the filtered reaction solution, add 1.00 mL of acetylacetone buffer (0.25%, wt) to it, fix the volume to 10.00 mL with deionized water, heat it in a water bath at 91 °C for 6 min, take it out, and measure the UV absorbance of the reaction solution after it is cooled to room temperature.

2.4 Theoretical model and calculation method

Based on the first principle plane wave ultra soft pseudopotential method, the crystal supercell models of different Bi based catalysts are established,[32] as shown in Fig. 1. The energy band structure, DOS and PDOS[33] of different catalyst supercells are compared, and various influencing factors are analyzed to provide a theoretical basis for the activity evaluation of Bi based catalysts.[34]

Based on DFT, the optical properties are calculated on Mede A platform. Considering the spin polarization effect, the pseudopotential of conservative norm is selected for structural optimization and electronic calculation.[35] Taking BiVO$_4$ as an example,[36] in the process of energy band calculation, the optimized K point is set to $3 \times 3 \times 3$. The cut-off energy is 571.40 eV and the electron energy is 1.0×10^{-6} eV, the maximum
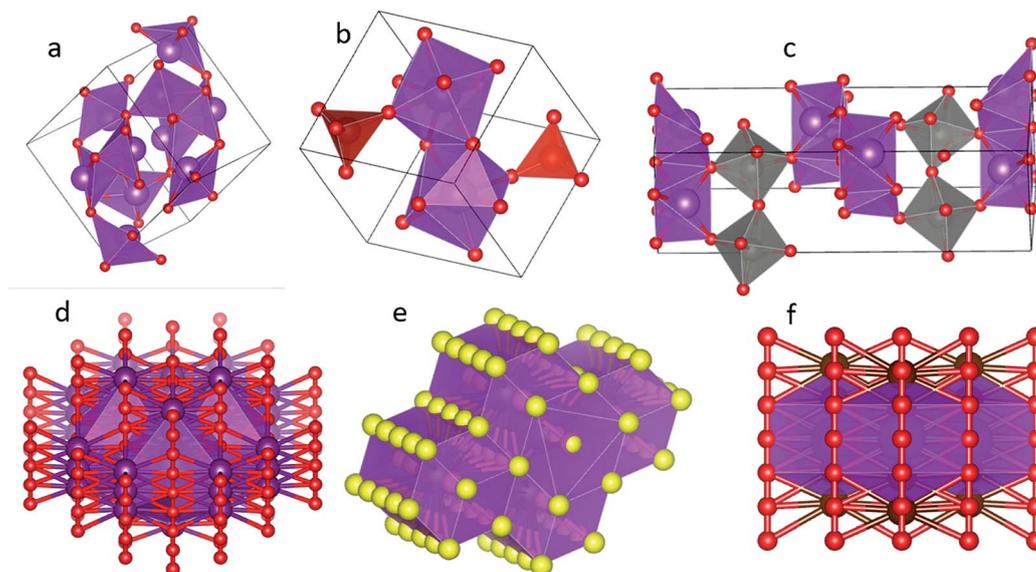

Fig. 1 Supercell model diagram of Bi$_2$O$_3$ (a), BiVO$_4$ (b), Bi$_2$WO$_6$ (c), BiOI (d), Bi$_2$S$_3$ (e), BiOBr (f) crystal.

displacement is 0.001 A, the accuracy of interatomic interaction force is 0.03 eV nm^{-1}, and the accuracy of crystal internal stress is 0.05 GPa.

3. Results and discussion

3.1 Material characterization

Fig. 2 shows the SEM of different Bi based catalysts. The specific analysis is as follows: Bi_2O_3 (a) is an irregular nano microsphere with rock like morphology and rich porous structure, and the diameter of micropores on the surface is about 50 nm; $BiVO_4$ (b) catalyst is formed by the accumulation of irregular flake nano-particles. The nanoparticles have a flake structure and uniform particle size, about 300 nm; Bi_2WO_6 (c) is flake particles with uniform morphology. After spatial overlap, it forms a nano flower structure with layer gap, which increases its specific surface area; BiOI (d) is a nanospherical structure formed by stacking rod-shaped particles with uniform morphology,[37] and the diameter of the nanosphere is 2–3 μm; the diameter of nanorod particles is about 20 nm and the length is about 300 nm; Bi_2S_3 (e) presents a spherical nanostructure with uniform diameter,[38] and the particle size is about 20–50 nm; BiOBr (f) is composed of relatively regular plate-like nano-particles. By comparing the SEM of six catalysts, it is found that their morphology is representative, which provides a theoretical basis for better exploring the application of Bi based catalysts in photocatalytic degradation of formaldehyde solution.

The functional groups of chemical bonds in various Bi based catalyst crystals were analyzed by FT-IR (Fig. 3a). According to Fig. 3, wide absorption peaks appeared near 3342 cm^{-1} and 1623 cm^{-1}, corresponding to the stretching vibration of H–O–H and O–H with strong hydrogen bond and the bending vibration of H–O–H, which may be caused by the physical adsorption of water in the air on the surface of nanocrystalline samples, The absorption peak near 1385 cm^{-1} is the C=O characteristic stretching vibration peak of CO_2 adsorbed in the air on the sample surface. The strong absorption peak of Bi_2O_3 near 447 cm^{-1} is the characteristic absorption peak of Bi_2O_3;[39] the absorption band of 540–850 cm^{-1} in the FT-IR of $BiVO_4$ is caused by the stretching and bending vibration of V–O in Bi–O and VO_4^{3-} tetrahedron; in Bi_2WO_6 crystal, the absorption of about 730 and 580 cm^{-1} corresponds to the stretching vibration of Bi–O and W–O, and the wide absorption peak at 734 cm^{-1} corresponds to the stretching vibration of W–O and the bridging stretching vibration of W–O–W; the characteristic absorption peak of BiOI crystal appeared at 486 cm^{-1}; the absorption peak of Bi_2S_3 at 618 cm^{-1} is the characteristic absorption peak of Bi–S bond; the absorption peak of BiOBr at 642 cm^{-1} is the stretching vibration peak of Bi–O, and the peak near 585 cm^{-1} belongs to the characteristic peak of BiOBr material, the stretching vibration peak of Bi–O bond.

The N_2 adsorption desorption isothermal curve of Bi based catalyst is shown in Fig. 3b, and the pore size distribution is shown in Fig. 3c. As shown in Fig. 3b, the isotherms of all samples conform to type IV isotherms. At high relative pressure (P/P_0), Bi based catalyst has H1 ring structure and particles gather uniformly. Among them, BiOI shows a high specific surface area of 25.93 m^2 g^{-1}. The other Bi based catalysts have little difference in Bi surface area; Table 1 shows the specific surface area, pore volume and pore diameter of Bi based
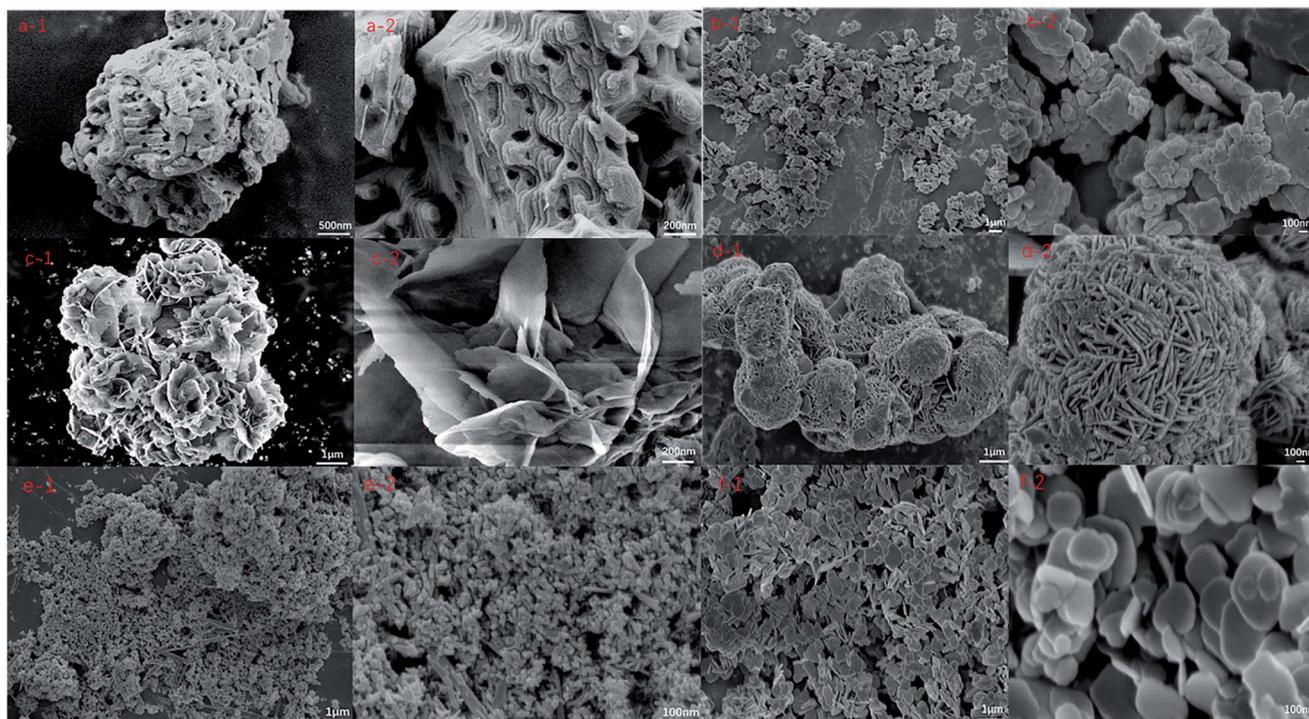

Fig. 2 SEM of Bi_2O_3 (a-1,2), $BiVO_4$ (b-1,2), Bi_2WO_6 (c-1,2), BiOI (d-1,2), Bi_2S_3 (e-1,2), BiOBr (f-1,2) crystals.

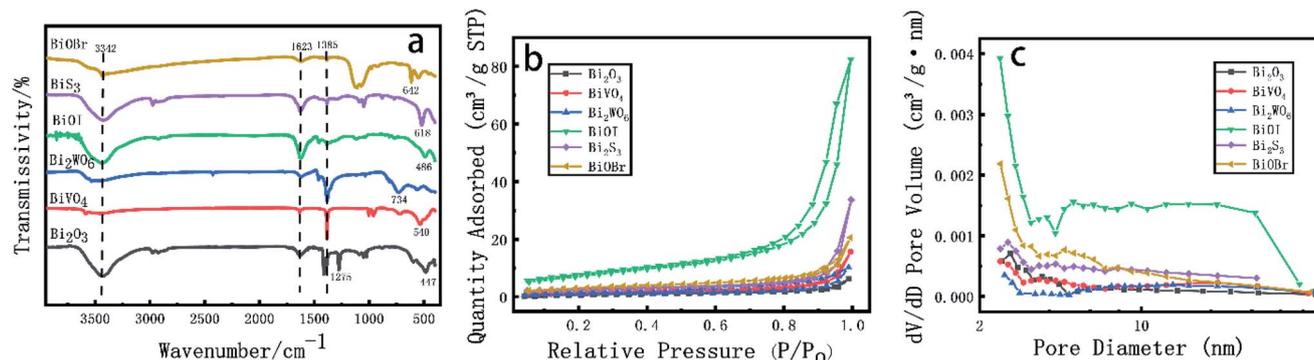© 2022 The Author(s). Published by the Royal Society of Chemistry

Fig. 3 (a) FT-IR spectra of Bi-based catalysts; (b) N_2 adsorption–desorption isotherms of Bi-based catalysts, (c) pore size distribution of Bi-based catalysts.

Table 1 Specific surface area, pore volume and pore size distribution of Bi-based catalysts

	Bi_2O_3	$BiVO_4$	Bi_2WO_6	$BiOI$	Bi_2S_3	$BiOBr$
Surface area ($m^2\ g^{-1}$)	3.2949	5.4018	4.0925	25.9333	8.5987	11.48
Pore volume ($cm^3\ g^{-1}$)	0.00963	0.01576	0.01493	0.12746	0.05179	0.03183
Pore size (nm)	16.0566	24.4777	25.5395	20.7095	11.8076	16.11

catalyst. It can be seen from Table 1 and Fig. 3C that the pore volume of Bi based catalyst is, and the pore diameter is mainly about 20 nm. It is a mesoporous material. $BiVO_4$ and Bi_2WO_6 have large pore diameters, 24.48 and 25.94 nm; in the experiment of photocatalytic degradation of formaldehyde, larger specific surface area can increase the effective loading of active ingredients, and the appropriate void volume and pore size distribution can make the formaldehyde molecules enter the pores of the catalyst more smoothly, provide more active sites for the degradation of formaldehyde and speed up the degradation rate.

As the macroscopic embodiment of the third-order nonlinear optical effect of the crystal, Raman laser characteristics occupy a certain position in the study of the crystal. As shown in Fig. 4, some basic studies on the Raman characteristics of Bi based catalysts were carried out. During the determination, the central excitation wavelength of Bi_2O_3, $BiVO_4$, Bi_2WO_6, BiOI and Bi_2S_3 was 532 nm and the central excitation wavelength of BiOBr was 540 nm. The peak centers observed by Bi_2O_3 were 320 and 453 cm^{-1} respectively; the peak centers observed by $BiVO_4$ were 355 and 813 cm^{-1}, respectively; the peak centers observed by Bi_2WO_6 were 300, 717 and 813 cm^{-1}, respectively; the peak centers observed by BiOI were 313 and 448 cm^{-1}, respectively; the peak centers observed by Bi_2S_3 are 262, 408 and 927 cm^{-1} respectively, and the peak centers observed by BiOBr are 113 and 266 cm^{-1} respectively. The Raman peaks of the above catalysts accord with the Raman characteristics of these substances. The Raman peaks of 1041 cm^{-1} (Bi_2O_3), 1031 cm^{-1} (Bi_2WO_6) and 1088 cm^{-1} (Bi_2S_3) may be the peak response signal caused by the anhydrous ethanol reagent selected when processing the sample.

Fig. 5a shows the full XPS spectrum of Bi based catalyst. It can be seen from the figure that the elements contained in the catalyst include Bi, O, W, V, Br, I and S, and the response of 284.4 eV is the standard peak of C. For six different Bi based catalysts, Bi 5d, Bi 5s, Bi 4f, Bi 4d and Bi 4p appear at 24.0, 160.4, 162.3, 464.0 and 679.0 eV respectively. The two symmetrical peaks of Bi 4f7/5 and Bi 4d5/3 are located at 157.0, 162.3 eV and 440.0, 464.0 eV respectively, which belong to the surface of the catalyst. For O, the binding energy of O 1s is 544.9 eV; the standard peak binding energies of W 4f and W 4d were 32.3 eV and 243.1 eV, respectively; the binding energy of V 2p standard peak in catalyst $BiVO_4$ is 519.0 eV; in the catalyst BiOI, the binding energies of 48.5, 185.5 and 619.2 eV correspond to 4d, 4s and 3d5/3 orbitals of I, respectively; the standard peak binding energies of 3d, 3p and 3s contained in the catalyst BiOBr were 68.5, 187.8 and 255.0 eV respectively; the binding energy of catalyst Bi_2S_3 at 229 eV corresponds to the S 2s orbital. By analyzing the XPS full spectrum of Bi based catalyst, a series of Bi based compounds were obtained by combining elements such as W, V, Br, I and S with O and Bi, which also provided the feasibility for the photocatalytic degradation experiment.

Fig. 5b shows the XRD diffraction pattern of Bi based catalyst. The obtained pattern is compared with the standard card by jade software (see Table 2 for the information of standard card and characteristic peak). It is found that the obtained Bi based catalyst shows good crystal form. Among them, Bi_2O_3 is in 2θ the diffraction peaks at 26.91°, 33.24° and 46.34° are sharp for (121), (203) and (221),[40] respectively, indicating that the Bi_2O_3 crystal prepared by calcination has good crystallinity; the most exposed faces of $BiVO_4$ crystal are (013) and (112), which correspond to 2θ it is 28.81° and 28.95°, and the diffraction peak at is attributed to the expansion and bending vibration of V–O,[41] indicating that the prepared $BiVO_4$ crystal has high crystallinity and no impurity peak, indicating that the purity of the product is high; similarly, for Bi_2WO_6 crystal, the crystal planes (113)
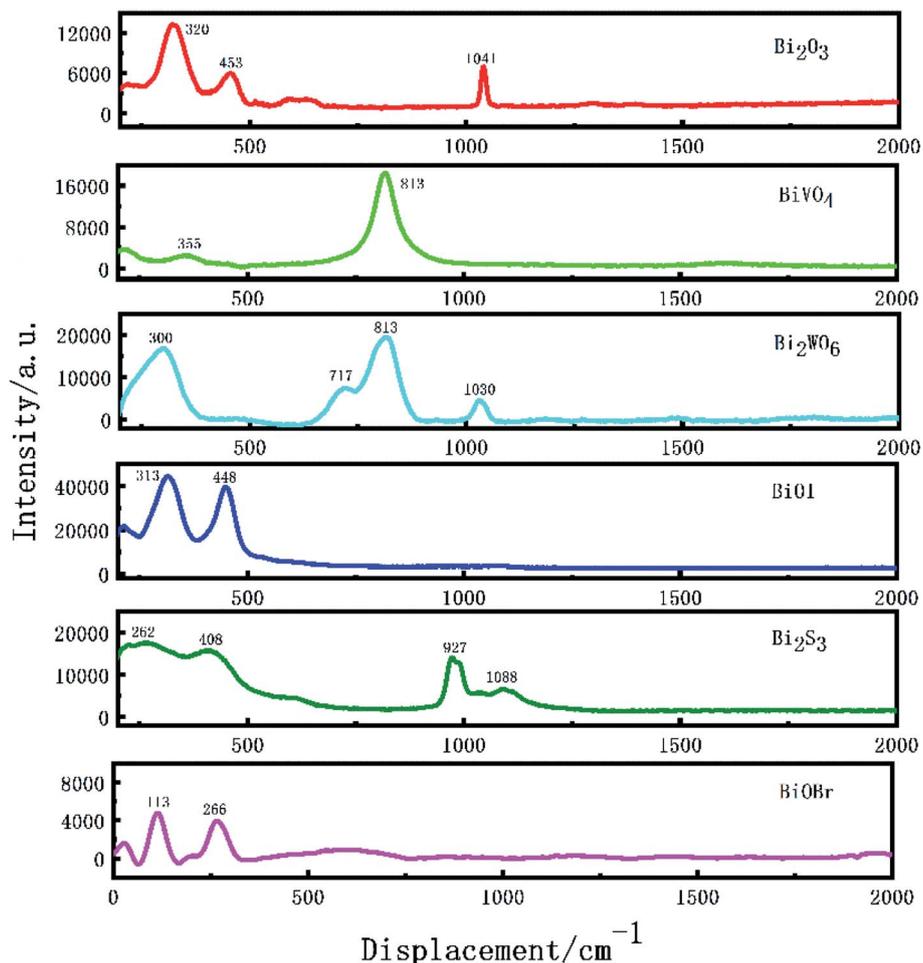
Fig. 4 Raman spectra of Bi-based catalysts.

and (200) exposed at the characteristic peaks of 28.31° and 32.93° belong to the stretching vibration of Bi–O and W–O, and some weak diffraction peaks indicate the process of forming Bi_2WO_6 nanocrystals; due to temperature and other reasons, the crystal structure growth is incomplete and the crystallinity is low; the main characteristic peaks of BiOI crystal are 29.74°, 31.74°, 45.49° and 55.30°, and the crystal planes represented are (012), (110), (220) and (122) respectively.[42] The sharp peak type
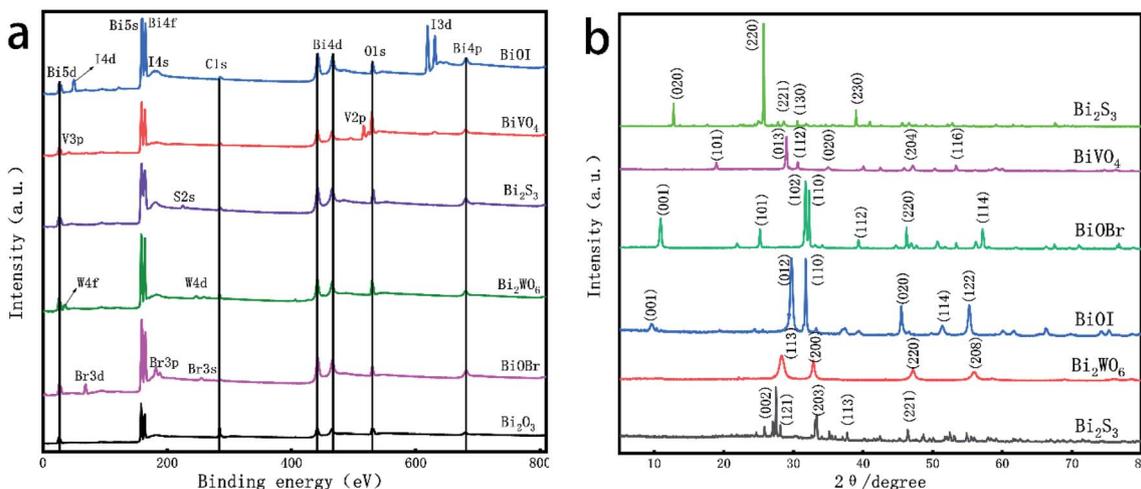

Fig. 5 (a) XPS spectra of Bi-based catalysts; (b) XRD patterns of Bi-based catalysts.

Table 2 XRD standard cards and characteristic peak information of Bi-based catalysts

	JCPDS	2-Theta (°)
Bi_2O_3	71–0465	25.75, 26.91, 27.39, 33.03, 33.24, 37.61, 46.34, 52.37, 54.797
$BiVO_4$	83–1700	18.98, 18.67, 28.81, 28.95, 30.53, 35.21, 46.72, 53.28, 59.67
Bi_2WO_6	73–1126	28.31, 32.80, 32.93, 46.98, 47.16, 55.68, 56.00
BiOI	73–2062	9.68, 29.74, 31.74, 45.49, 51.49, 55.30
Bi_2S_3	75–1306	15.74, 17.658, 22.47, 25.04, 28.732, 31.92, 33.05, 35.755, 40.09, 46.65, 52.92, 59.31
BiOBr	78–0348	10.91, 31.72, 33.13, 39.32, 46.24, 50.66, 53.38, 57.16

indicates that the synthesized BiOI has excellent crystallinity; in the XRD diffraction pattern of Bi_2S_3, 2θ the characteristic peak at 28.73° is sharp, indicating that the bending vibration of Bi–S bond has a great influence on the crystallinity of Bi_2S_3 crystal; BiOBr crystal has many characteristic peaks in 2θ the characteristic peaks at 10.91°, 31.72°, 33.12° and 46.24° are sharp and clear, indicating that the BiOBr prepared by hydrothermal method has high crystallinity.[12]

3.2 Catalytic performance of catalyst

In the experiment of photocatalytic degradation of formaldehyde aqueous solution, the degradation effects of different Bi based catalysts on formaldehyde aqueous solution with mercury lamp and xenon lamp as light source were investigated.[43] The prepared Bi based catalyst was ground to powder and evenly dispersed in 20.00 mL formaldehyde aqueous solution (0.5 mg mL^{-1}), stir for 60 min under dark condition to reach the equilibrium of adsorption and desorption. The degradation experiment was carried out under the condition of sufficient light source. 0.50 mL sample was taken out from the reaction solution every 1 h, and the content of formaldehyde in the solution was determined by UV spectrophotometer.

It can be seen from Fig. 6d that the UV absorbance value of the reaction solution at 413 nm decreases with the extension of time. As can be seen from Fig. 6a, in the dark reaction process, the adsorption capacity of catalyst for formaldehyde in the solution is very small, and the adsorption capacity of $BiVO_4$ is the highest, reaching 3.61%. Six different catalysts showed good degradation under the irradiation of mercury lamp. The degradation rate can be obtained from formula (1-1) (where V is the degradation rate, A_0 is the absorbance of the non degraded solution, and A is the absorbance of the degraded solution). Among them, the degradation efficiency of Bi_2O_3 and BiOBr
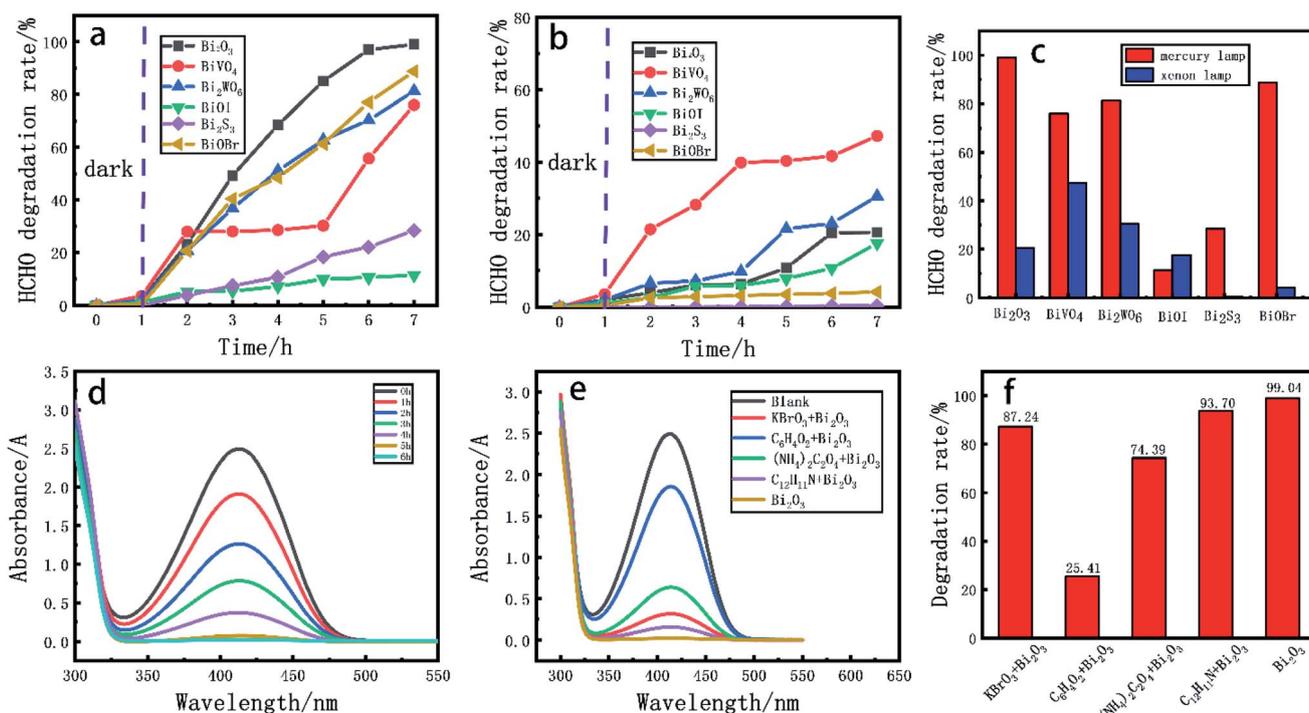

Fig. 6 (a) Degradation of formaldehyde aqueous solution by bi-based catalyst in mercury lamp; (b) solution of formaldehyde by bi-based catalyst in xenon lamp; (c) degradation rate of bi-based catalyst for formaldehyde solution under mercury lamp and xenon lamp for 6 h; (d) Bi_2O_3 catalyst for degradation of formaldehyde aqueous solution by mercury lamp within 6 h; (e) free radical quenching experiment using Bi_2O_3 as catalyst and mercury lamp as light source; (f) effect of different radical quenching groups on photocatalytic degradation efficiency of formaldehyde aqueous solution.

Table 3 Apparent kinetic characteristics of Bi-based catalyst for degradation of formaldehyde aqueous solution

| | dC/dt | | | | | | | | | | | |
| | Xenon lamp | | | | | | Mercury lamp | | | | | |
Time/h	Bi_2O_3	$BiVO_4$	Bi_2WO_6	BiOI	Bi_2S_3	BiOBr	Bi_2O_3	$BiVO_4$	Bi_2WO_6	BiOI	Bi_2S_3	BiOBr
1	0.0090	0.0095	0.0120	0.0064	0.0002	0.0008	0.0296	0.0168	0.0236	0.0033	0.0120	0.0263
2	0.0088	0.0087	0.0119	0.0062	0.0002	0.0008	0.0195	0.0167	0.0188	0.0033	0.0116	0.0197
3	0.0088	0.0073	0.0116	0.0062	0.0002	0.0008	0.0121	0.0166	0.0145	0.0032	0.0112	0.0171
4	0.0083	0.0072	0.0100	0.0060	0.0002	0.0008	0.0057	0.0162	0.0111	0.0032	0.0102	0.0128
5	0.0074	0.0071	0.0098	0.0059	0.0002	0.0008	0.0011	0.0103	0.0088	0.0031	0.0097	0.0076
6	0.0074	0.0064	0.0089	0.0054	0.0002	0.0008	0.0004	0.0056	0.0056	0.0031	0.0089	0.0037

reaches 99.04% and 88.80% respectively, and the degradation efficiency of $BiVO_4$ and Bi_2WO_6 reaches 76.23% and 81.29% respectively; Fig. 6b shows the degradation effect of different catalysts on formaldehyde aqueous solution under xenon lamp. It can be seen from Fig. 6c that under xenon lamp atmosphere, the degradation rates of $BiVO_4$ and Bi_2WO_6 to formaldehyde within 6 h reach 47.29% and 30.59% respectively, but the degradation effect of other Bi based catalysts under xenon lamp is not ideal.

$$V = \frac{A_0 - A}{A_0} \times 100\% \quad (1\text{-}1)$$

$$\frac{dC}{dt} = -k'a^* \times mC \quad k' = \frac{k}{a^*m} \quad (2\text{-}2)$$

The apparent kinetic characteristics of photocatalytic degradation of formaldehyde aqueous solution were analyzed according to formula (2-2),[44] where a^* is the ratio of catalyst specific surface area to mass, m is catalyst mass/solution volume, and k is obtained from normalized concentration data. From Table 3, Fig. 8e, you can see that light in the experiments of catalyst to formaldehyde degradation rate affected by the molecular diffusion of formaldehyde, and the diffusion process is associated with the specific surface area of catalyst, the rate at which is suitable for the specific surface area of light catalysis have played an important role in promoting, formaldehyde concentration, the largest $BiVO_4$ constant and reaction kinetics of the Bi_2WO_6 has the highest, 0.023, 0.029 min^{-1}.

Bi_2O_3 is a semiconductor material with various forms and shows good light response performance. However, due to the
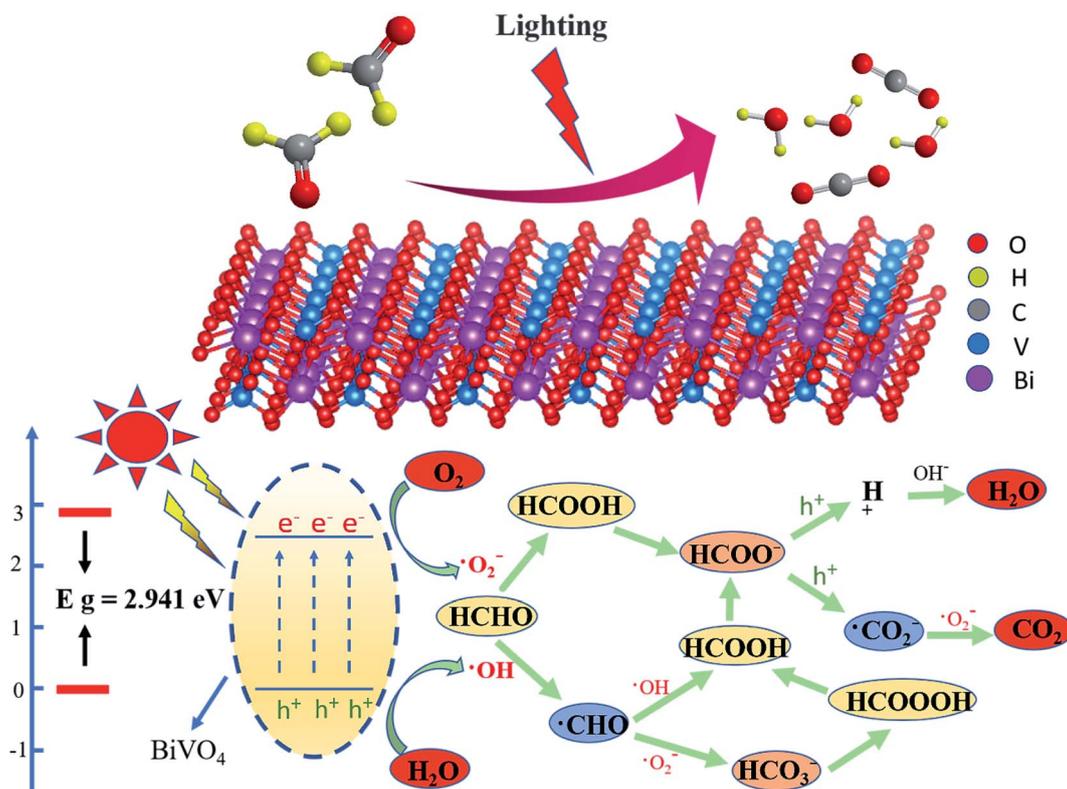
Fig. 7 Mechanism of photocatalytic degradation of formaldehyde aqueous solution (taking $BiVO_4$ as an example).

problem of rapid recombination of light induced electron and hole pairs, Bi_2O_3 has poor photocatalytic decomposition efficiency of organic pollutants, and does not show better degradation efficiency in the process of degradation of formaldehyde aqueous solution by xenon lamp. $BiVO_4$ can have an absorption band in the ultraviolet region and in the visible region ($\lambda > 420$ nm). This is due to the partial deformation of Bi–O caused by the lone pair electrons of Bi^{3+} in 6s2 orbit. The absorption in the visible region of $BiVO_4$ is the transition of electrons from the Bi 6s orbit or the hybrid orbit of Bi 6s and O 2p to the V 2p orbit. The absorption in UV region mainly depends on the electronic transition from O 2p orbital to V 2p orbital. Therefore, $BiVO_4$ can show better catalytic efficiency in both UV and visible regions; the same as $BiVO_4$ crystal, Bi_2WO_6 crystal is easy to transition electrons from the hybrid orbital of Bi 6s and O 2p to the W 6s orbital under light conditions due to the existence of W element.

Which shows excellent catalytic performance in the visible and ultraviolet regions. For bismuth halide oxide, the absorption of BiOI can not cover the whole visible spectrum, and it has an anisotropic layered structure, which is easy to be photogenerated and carriers are easy to be combined, resulting in low photocatalytic efficiency; similarly, as a semiconductor material with narrow band gap, Bi_2S_3 is limited to a certain extent in the process of photocatalytic degradation of organic compounds;[45] the energy band of BiOBr is mainly composed of hybrid orbitals of Br 4p, O 2p and Bi 6s orbitals. At the same time, the existence of Bi element will raise the low conduction band (CBM)

position, increase the band gap, promote carrier transfer, and show excellent catalytic performance under ultraviolet light.

In order to further explore the mechanism of photocatalytic degradation of formaldehyde aqueous solution, we carried out free radical quenching experiments, as shown in Fig. 6-E. When Bi_2O_3 was used as catalyst and mercury lamp was used as light source, potassium bromate ($KBrO_3$) was used as electron capture agent, p-benzoquinone ($C_6H_4O_2$) was used as $\cdot O_2^-$ capture agent ammonium oxalate ($(NH_4)_2C_2O_4$) was used as hole trapping agent and diphenylamine ($C_{12}H_{11}N$) was used as $\cdot OH^-$ trapping agent. According to Fig. 6f, it can be found that the degradation rate of formaldehyde decreased by 11.8%, 73.63%, 24.65% and 5.34% respectively after adding free radical capture agent. The above results show that $\cdot O_2^-$ plays an important role in the photocatalytic degradation of formaldehyde aqueous solution. Similarly, holes also play a certain role in the degradation process. Based on this, We reasonably speculated the mechanism of photocatalytic degradation of formaldehyde aqueous solution,[46] as shown in the Fig. 7.

The path and mechanism of photocatalytic degradation of formaldehyde aqueous solution were reasonably speculated;[47] when the light source irradiates the semiconductor surface, electron transition will occur and electron hole pairs will be generated. Electrons and holes can oxidize and reduce H_2O and O_2 to $\cdot OH$ and $\cdot O_2^-$ the contact between HCHO molecule and $\cdot OH$ will produce $\cdot CHO$. At the same time, $\cdot CHO$ will produce HCOOH and HCO_3^- respectively under the action of $\cdot OH$ and $\cdot O_2^-$. Among them, HCO_3^- ions will generate HCOOOH
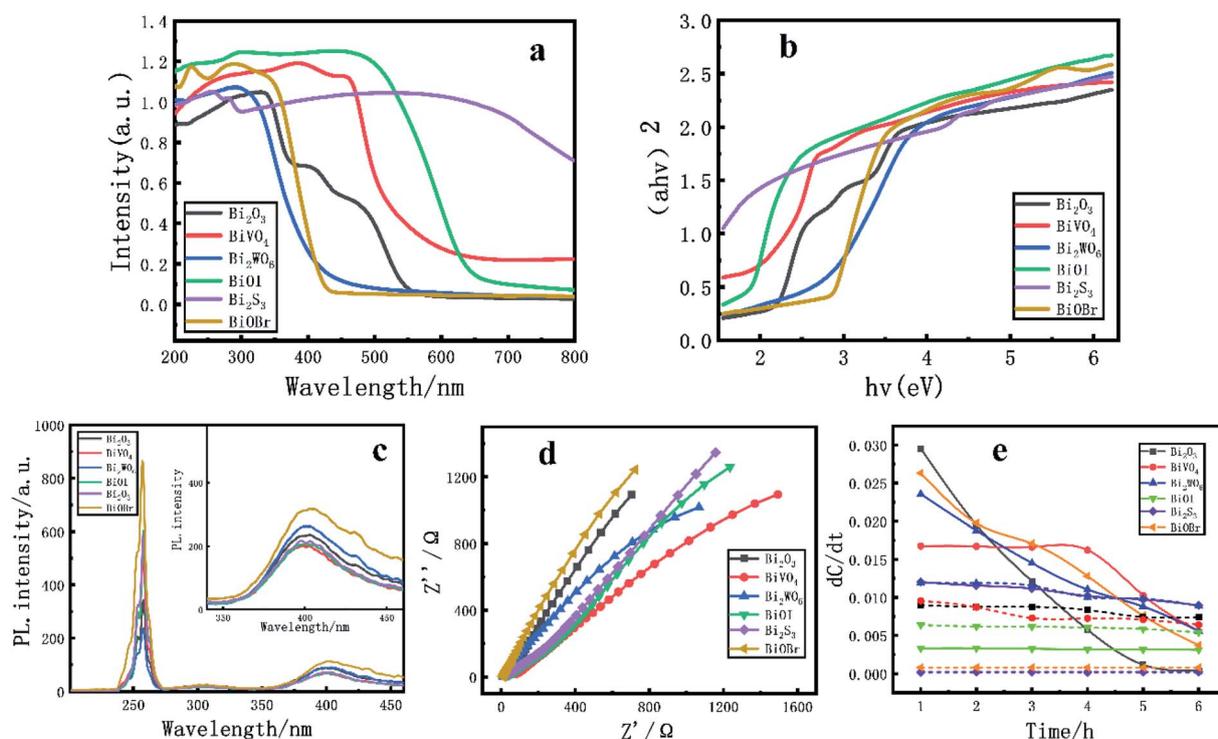

Fig. 8 (a, b) UV-Vis DRS spectra of Bi-based catalysts; (c) photoluminescence spectra (PL) of Bi-based catalysts; (d) EIS of Bi-based catalysts; (e) apparent kinetic characteristics of Bi-based catalyst for degradation of formaldehyde aqueous solution (solid line is photocatalytic formaldehyde under mercury lamp, short line is photocatalytic formaldehyde under xenon lamp).

molecules after hydrogenation, this molecule interacts with HCHO to produce HCOOH; in addition, HCHO molecules are oxidized to HCOOH under the action of $\cdot O_2^-$. $HCOO^-$ produced by HCOOH molecule after losing H^+ generates H^+ and $\cdot CO_2^-$ under the action of H^+, and H^+ and $\cdot CO_2^-$ generate our final products H_2O and CO_2 under the action of OH^- and $\cdot O_2^-$ respectively. Based on the results of free radical quenching experiment, the mechanism of photocatalytic formaldehyde is more inclined to the path of HCHO directly generating HCOOH under the action of $\cdot O_2^-$, and then H_2O and CO_2 under the joint action of H^+, OH^- and $\cdot O_2^-$.

3.3 Activity evaluation of catalyst

The photocatalytic performance is closely related to the ability to absorb light. Therefore, the reflection and absorption characteristics of the catalyst are tested by UV-Vis DRS,[48] and the results are shown in Fig. 8-a and b. Different Bi based catalysts have strong absorption in the visible and ultraviolet regions, and all catalysts have steep absorption boundary phenomena in the ultraviolet and visible spectra. $BiVO_4$ and Bi_2WO_6 have long absorption edges in the visible region. Because the transition of the catalyst in the visible absorption is caused by the electronic transition of the energy band energy level structure. It shows that the above catalysts have relatively reasonable energy band structure and strong light absorption capacity.

Fig. 8-c shows the PL spectra of different Bi based catalysts.[49,50] When the atoms on the light-emitting substrate in Bi based catalyst particles are excited and collided by excited light particles with certain energy, the ionized free electrons will produce excitation ionization after colliding with other atoms. When the excited or ionized atoms return to the stable state, the fluorescence absorption peak will appear. The intensity of the fluorescence peak indicates the photogenerated electron hole recombination rate. The lower the intensity, the lower the recombination efficiency. When the excitation wavelength is 240 nm, it can be found that different catalysts have strong fluorescence absorption peaks at 405 nm. Through the spectrum, it is found that BiOBr shows strong fluorescence absorption, and the PL emission spectrum intensity of the other Bi based catalysts has little difference. Among them, $BiVO_4$ has weak fluorescence absorption and shows high photogenerated charge separation efficiency.

The EIS of Bi based catalyst was determined under the conditions of visible light and 0.7 V *vs.* Ag/AgCl. In Fig. 8-d, Z' represents the real part of the measured impedance, Z' represents the negative number of the imaginary part of the measured impedance, and the radius of the arc reflects the charge transmission resistance between the semiconductor and electrolyte interface. In general, the smaller the radius means that the photogenerated electrons and holes are effectively separated and the photogenerated electrons migrate rapidly.[51] It is found that BiOBr has a larger arc radius, while $BiVO_4$ has a smaller arc radius and lower charge transfer resistance, that is, it has higher electric core separation efficiency and faster

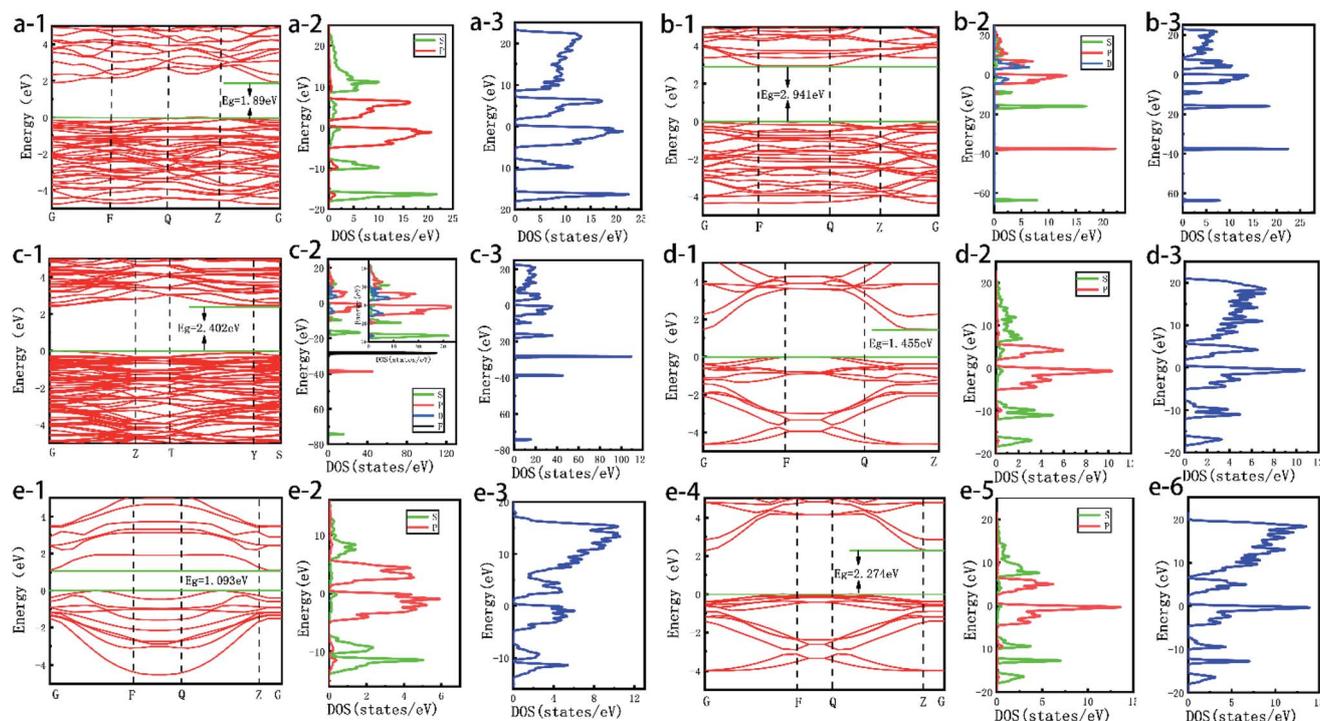**Fig. 9** Energy band structure of Bi_2O_3 crystal (a-1), PDOS (a-2), DOS (a-3); energy band structure of $BiVO_4$ crystal (b-1), PDOS (b-2), DOS (b-3); the band structure diagram of Bi_2WO_6 crystal (c-1), PDOS (c-2), DOS (c-3); energy band structure diagram of BiOI crystal (d-1), PDOS (d-2), DOS (d-3); the band structure diagram of Bi_2S_3 crystal (e-1), PDOS (e-2), DOS (e-3); energy band structure diagram of BiOBr crystal (f-1), PDOS (f-2), DOS (f-3).

photogenerated electron migration rate, and its photochemical properties are enhanced.

In order to further reveal the effect of the optical properties of Bi based catalyst on the activity of the catalyst, the energy band structure of the photocatalyst was calculated by DFT. The results are shown in Fig. 9a–f-1. The band gaps of Bi_2O_3, $BiVO_4$, Bi_2WO_6, BiOI, Bi_2S_3 and BiOBr catalysts are 1.89, 2.941, 2.402, 1.455, 1.093 and 2.274 eV respectively.[52] It can be found that the band gaps calculated by theory are roughly consistent with the experimental results. At the same time, most Bi based semiconductor photocatalysts not only have narrow band gap, but also have positive valence band position. That is, photogenerated holes have strong oxidation ability and are very suitable for photocatalytic reaction. Among them, Bi_2O_3, $BiVO_4$, Bi_2WO_6 and BiOBr have appropriate energy band structures.[32,34] At the same time, the DOS and PDOS of Bi based catalysts are calculated in Fig. 9a–f-2,3. The results

show that the density of states of most Bi based catalysts are similar, which is mainly provided by the hybridization of s orbital and p orbital, the density of states at the top of the valence band (−25 eV to 0 eV) is mainly contributed by the 6s orbitals of O and Bi; the contribution of the DOS at the bottom of the conduction band (2 eV to 20 eV) mainly comes from the 6p orbital of Bi and the 2p orbital of O. However, for $BiVO_4$ and Bi_2WO_6 crystals, in addition to the DOS contributed by the s and p orbitals of Bi and O, the d and f orbitals of V and W also contribute a certain DOS to the above two catalysts. The optical properties of $BiVO_4$ and Bi_2WO_6 crystals play a key role. Thus, it shows excellent photocatalytic activity in the visible light range.[53]

In order to further study the effect of hybrid orbitals of different elements in Bi based catalyst on crystal optical properties,[54] the PDOS[55] of different elements were calculated in the figure. In Fig. 10a-1 and a-2, Bi-PDOS and O-PDOS are shown

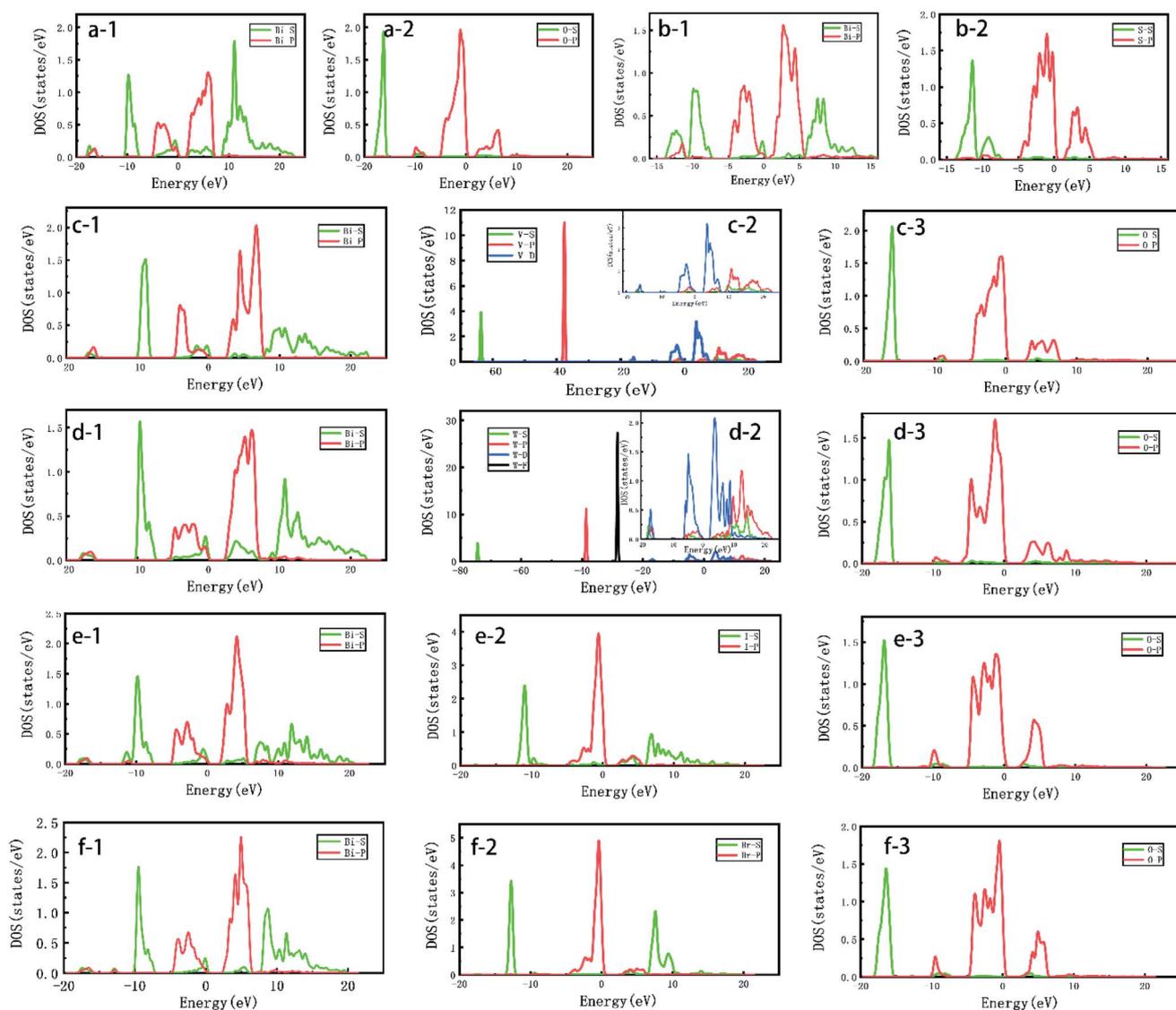**Fig. 10** PDOS of different elements in Bi-based catalysts: Bi_2O_3: Bi-PDOS (a-1), O-PDOS (a-2); Bi_2S_3: Bi-PDOS (b-1), S-PDOS (b-2); $BiVO_4$: Bi-PDOS (c-1), V-PDOS (c-2), O-PDOS (c-3); Bi_2WO_6: Bi-PDOS (d-1), W-PDOS (d-2), O-PDOS (d-3); BiOI: Bi-PDOS (e-1), I-PDOS (e-2), O-PDOS (e-3); BiOBr: Bi-PDOS(f-1), Br-PDOS(f-2), O-PDOS(f-3).

respectively. It can be seen that the s and p orbitals of Bi element provide most of the DOS for Bi_2O_3. The s and p orbitals of O element are mainly located at -17.0 eV and -2.0 eV, belonging to the range of valence band top, that is, the participation of O element has a certain impact on the position and size of energy band of Bi_2O_3; the same as Bi_2O_3 is Bi_2S_3 crystal. The s and p orbitals of Bi element also increase most of the DOS for the catalyst. However, unlike Bi_2O_3, the p orbitals of S element provide a certain density of states for Bi_2S_3 at 1.0–6.0 eV, which affects the position of its low conduction band, resulting in a significant reduction of its band gap to 1.093 eV, which has a serious impact on the photochemical properties. In the study of bismuth oxyhalide, as shown in Fig. 10-e, f-1 is Bi-PDOS, Fig. 10-e, f-2 are I-PDOS and Br-PDOS respectively, and Fig. 10-e and f-3 are O-PDOS. Comparing the contribution of s and p orbitals of each element in the two catalysts to DOS, it can be found that the s orbitals of Bi element contribute more DOS to BiOBr at 6.0–12.0 eV, reaching 1.2 eV, which is 0.7 eV higher than that of BiOI at the same time. The DOS value of the s orbitals of the same Br element is higher than that of I element at 8.0 eV, which is nearly 1.7 eV higher. The above situation leads to the difference in the degradation of organic matter between the two bismuth halides under ultraviolet light, and BiOBr shows more excellent photochemical properties. $BiVO_4$ and Bi_2WO_6 are Bi based catalysts with excellent performance in degrading organic matter under visible light. Fig. 10-d, e-1, 2 and 3 show Bi-PDOS, V-PDOS and O-PDOS of $BiVO_4$ catalyst and Bi-PDOS, W-PDOS and O-PDOS of Bi_2WO_6 catalyst respectively. It can be seen from the figure that the conduction band region on the surface of $BiVO_4$ crystal is contributed by the s and p orbitals of Bi, the s orbitals of O and the p and d orbitals of V. the bottom region of the conduction band is mainly occupied by the p orbitals of Bi and the d orbitals of V. the DOS contribution of the valence band region mainly comes from the s and p orbitals of Bi and the s and p orbitals of O. The s and p orbitals of V do not contribute much to the DOS of the valence band region. The above results show that, the introduction of V element has a great influence on the valence band region of $BiVO_4$ crystal, which makes it have a more suitable energy band structure and optimizes its photochemical properties; the DOS contribution of Bi_2WO_6 crystal surface mainly comes from the s and p orbitals of Bi, the s and p orbitals of O and the p and d orbitals of W. the DOS in the conduction band bottom region mainly comes from the s orbitals of Bi and the d orbitals of W. At the same time, the DOS in the valence band top region is also largely occupied by the d orbitals of W, which indicates that w element dominates the energy band size and position of Bi_2WO_6 crystal, making its band gap reach 2.402 eV. Therefore, it shows more excellent electrochemical properties. However, compared with $BiVO_4$ crystal, the hybridization of s and p orbitals of W makes its electron distribution more dispersed, which affects its photochemical properties to a certain extent.

4. Conclusions

Firstly, a series of Bi based catalysts were prepared by calcination and hydrothermal synthesis. XRD results showed that the

prepared catalyst had sharp and clear characteristic peaks and no impurity peaks, which showed that the prepared catalyst had good crystallinity and high purity, which could be confirmed by XPS and Raman results. Subsequently, the unique morphologies of different catalysts were characterized by SEM, and BET also confirmed that the prepared catalysts had high specific surface area.

In the experiment of photocatalytic degradation of formaldehyde aqueous solution, the degradation experiments were carried out under xenon lamp and mercury lamp respectively. The results showed that the experimental Bi based catalysts showed excellent degradation efficiency under ultraviolet light. At 6 h, Bi_2O_3, BiOBr, $BiVO_4$ and Bi_2WO_6 catalysts showed extremely strong degradation efficiency, reaching 99.04%, 88.80%, 76.23% and 81.29% respectively; in the visible light range, $BiVO_4$ and Bi_2WO_6 showed strong degradation effect, and the degradation rates of formaldehyde reached 47.29% and 30.59% respectively within 6 hours; at the same time, through the free radical quenching experiment, it can be found that when $C_6H_4O_2$ is used as $\cdot O_2^-$ capture agent, the degradation rate of formaldehyde decreases by 73.63%, indicating that $\cdot O_2^-$ plays an important role in the photocatalytic degradation of formaldehyde aqueous solution. Subsequently, the tests of PL, UV Vis and EIS showed that $BiVO_4$ and Bi_2WO_6 catalysts had excellent photochemical properties and showed strong activity under UV and visible light.

The energy bands, DOS and PDOS of Bi based catalysts were calculated based on DFT. Through the calculation of energy band structure, it is found that Bi_2O_3, $BiVO_4$, Bi_2WO_6 and BiOBr have appropriate energy band structure, and their band gaps are 1.89, 2.941, 2.402 and 2.274 eV respectively, which can show excellent photochemical properties in the ultraviolet region; in the calculation of DOS and PDOS, it is found that in the composition of DOS in the conduction band region of $BiVO_4$ and Bi_2WO_6, the d orbital of V and the d orbital of W occupy most positions, indicating that the of V and W have a great influence on the energy band position and size of the catalyst, making it have a more appropriate energy band structure and band gap, and show strong activity under ultraviolet and visible light. This result is also mutually confirmed with our experimental results.

Author contributions

Runquan Wang designs experiments, implements experiments, analyzes experimental data and writes papers; Yuerong Zhang data analysis, Wanping Chen catalytic degradation theory calculation; Yuan Tian, Kai Song, and Jiaxian Li provided assistance in sample delivery testing and experimental implementation.

Conflicts of interest

There are no conflicts of interest to declare.

References

1 D.-H. Zhuo, Q.-S. Chen, X.-H. Zhao, Y.-L. Jiang, J. Lu, Z.-N. Xu and G.-C. Guo, *J. Mater. Chem. C*, 2021, **9**, 7900–7904.

2 Z. Zhou, J. Yang, Q. Jiang, Y. Luo, D. Zhang, Y. Ren, X. He and J. Xin, *J. Mater. Chem. A*, 2016, **4**, 13171–13175.

3 M. Arumugam and M. Y. Choi, *J. Ind. Eng. Chem.*, 2020, **81**, 237–268.

4 A. Kubacka, M. Fernandez-Garcia and G. Colon, *Chem. Rev.*, 2012, **112**, 1555–1614.

5 A. Benhmid, K. V. Narayana, A. Martin, B. Lucke and M. M. Pohl, *Chem. Commun.*, 2004, 2416–2417, DOI: 10.1039/b410310f.

6 X.-H. Zhao, Q.-S. Chen, D.-H. Zhuo, J. Lu, Z.-N. Xu, C.-M. Wang, J.-X. Tang, S.-G. Sun and G.-C. Guo, *Electrochim. Acta*, 2021, 367.

7 Y. Yuan, Y. Huang, F. Ma, Z. Zhang, X. Wei and G. Zhu, *J. Mater. Sci.*, 2016, **51**, 6662–6673.

8 W. Li, X.-y. Liu, X.-s. Chu, F. Wang, Y.-y. Dang, T.-h. Ma, J.-y. Li and C.-y. Wang, *Environ. Sci.*, 2021, **8**, 3655–3664.

9 J. Wang, X. Xu, Y. Liu, Z. Wang, P. Wang, Z. Zheng, H. Cheng, Y. Dai and B. Huang, *ChemSusChem*, 2020, **13**, 3488–3494.

10 Z. Cui, X. Dong, Y. Sun, Y. Zhou, Y. Zhang and F. Dong, *Nanoscale*, 2018, **10**, 16928–16934.

11 H. Bahruji, M. Bowker, P. R. Davies and F. Pedrono, *Appl. Catal., B*, 2011, **107**, 205–209.

12 H. Li, J. Liu, T. Hu, N. Du, S. Song and W. Hou, *Mater. Res. Bull.*, 2016, **77**, 171–177.

13 L. Hao, H. Huang, Y. Zhang and T. Ma, *Adv. Funct. Mater.*, 2021, 31.

14 W. Li, F. Wang, X.-s. Chu, Y.-y. Dang, X.-y. Liu, T. Ma, J.-y. Li and C.-y. Wang, *Chem. Eng. J.*, 2022, 435.

15 W. Li, X.-s. Chu, F. Wang, Y.-y. Dang, X.-y. Liu, T.-h. Ma, J.-y. Li and C.-y. Wang, *Appl. Catal., B*, 2022, 304.

16 Z. Chen, F. Lv, R. Li, Z. Sun and Y. Zhang, *Mater. Res. Bull.*, 2019, **118**, 110514.

17 X. Li, Y. Sun, T. Xiong, G. Jiang, Y. Zhang, Z. Wu and F. Dong, *J. Catal.*, 2017, **352**, 102–112.

18 Q. Guo, Z. Ma, C. Zhou, Z. Ren and X. Yang, *Chem. Rev.*, 2019, **119**, 11020–11041.

19 J. Yang, Q. Shi, R. Zhang, M. Xie, X. Jiang, F. Wang, X. Cheng and W. Han, *Carbon*, 2018, **138**, 118–124.

20 M. T. Laciste, M. D. G. de Luna, N. C. Tolosa and M. C. Lu, *Chemosphere*, 2017, **182**, 174–182.

21 Y. Feng, B.-J. Huang, S.-S. Li, B.-M. Zhang, W.-X. Ji, C.-W. Zhang and P.-J. Wang, *J. Mater. Sci.*, 2015, **50**, 6993–6999.

22 J. Deng and Z.-Y. Zhao, *Comput. Mater. Sci.*, 2018, **142**, 312–319.

23 M. Yang, Y. Z. Luo, M. G. Zeng, L. Shen, Y. H. Lu, J. Zhou, S. J. Wang, I. K. Sou and Y. P. Feng, *Phys. Chem. Chem. Phys.*, 2017, **19**, 29372–29380.

24 C. Nguyen Van, T. H. Do, J.-W. Chen, W.-Y. Tzeng, K.-A. Tsai, H. Song, H.-J. Liu, Y.-C. Lin, Y.-C. Chen, C.-L. Wu, C.-W. Luo, W.-C. Chou, R. Huang, Y.-J. Hsu and Y.-H. Chu, *NPG Asia Mater.*, 2017, **9**, e357.

25 M. Choi, *Appl. Phys. Lett.*, 2021, 118.

26 Z. Zhang, Y. Lin and F. Liu, *Colloids Surf., A*, 2020, 590.

27 X. Lou, J. Shang, L. Wang, H. Feng, W. Hao, T. Wang and Y. Du, *J. Mater. Sci. Technol.*, 2017, **33**, 281–284.

28 D. Wu, S. Yue, W. Wang, T. An, G. Li, L. Ye, H. Y. Yip and P. K. Wong, *Appl. Surf. Sci.*, 2017, **391**, 516–524.

29 S. S. Imam, R. Adnan and N. H. Mohd Kaus, *J. Environ. Chem. Eng.*, 2021, **9**.

30 R. S. Lokhande, S. R. Thakur and P. A. Chate, *Optik*, 2020, 219.

31 Z. Wang, F. Xiong, Z. Zhang, G. Sun, H. Xu, P. Chai and W. Huang, *J. Phys. Chem. C*, 2017, **121**, 25921–25929.

32 H. Ahmad, A. Rauf, A. Ahmad, A. Ulhaq and S. Muhammad, *RSC Adv.*, 2021, **11**, 32330–32338.

33 W. Dan, K. Chang, Y. Zhang, Y. Wang, Q. Liu, Z. Wang, D. Ding, Y. Cui, C. Pan, Y. Lou, Y. Zhu and Y. Zhang, *Appl. Catal., B*, 2021, 299.

34 Y. Bi, Y. Yang, X.-L. Shi, L. Feng, X. Hou, X. Ye, L. Zhang, G. Suo, S. Lu and Z.-G. Chen, *J. Mater. Sci. Technol.*, 2021, **83**, 102–112.

35 R. Z. Huang, Y. Y. Wei, T. F. Gao, C. M. Li and C. H. Jiang, *Ceram. Int.*, 2021, **47**, 205–213.

36 L. d. Olmo, M. Dommett, I. H. Oevreeide, A. Walsh, D. Di Tommaso and R. Crespo-Otero, *J. Mater. Chem. A*, 2018, **6**, 24965–24970.

37 A. C. Mera, C. A. Rodríguez, M. F. Meléndrez and H. Valdés, *J. Mater. Sci.*, 2016, **52**, 944–954.

38 X. Li, Y. Wu, H. Ying, M. Xu, C. Jin, Z. He, Q. Zhang, W. Su and S. Zhao, *J. Alloys Compd.*, 2019, **798**, 628–634.

39 T. Hashimoto, H. Ohta, H. Nasu and A. Ishihara, *Int. J. Hydrogen Energy*, 2016, **41**, 7388–7392.

40 L. D. Geoffrion, D. Medina-Cruz, M. Kusper, S. Elsaidi, F. Watanabe, P. Parajuli, A. Ponce, T. B. Hoang, T. Brintlinger, T. J. Webster and G. Guisbiers, *Nanoscale Adv.*, 2021, **3**, 4106–4118.

41 W. Wang, P. J. Strohbeen, D. Lee, C. Zhou, J. K. Kawasaki, K.-S. Choi, M. Liu and G. Galli, *Chem. Mater.*, 2020, **32**, 2899–2909.

42 R. A. Jagt, T. N. Huq, K. M. Börsig, D. Sauven, L. C. Lee, J. L. MacManus-Driscoll and R. L. Z. Hoye, *J. Mater. Chem. C*, 2020, **8**, 10791–10797.

43 T. Cai, P. Zhang, X. Shen, E. Huang, X. Shen, J. Shi, Z. Wang and Q. Sun, *ACS Appl. Mater. Interfaces*, 2020, **12**, 37147–37154.

44 A. P. Reverberi, P. S. Varbanov, M. Vocciante and B. Fabiano, *Front. Chem. Sci. Eng.*, 2018, **12**, 878–892.

45 N. Mahuli, D. Saha and S. K. Sarkar, *J. Phys. Chem. C*, 2017, **121**, 8136–8144.

46 X. Li, H. Li, Y. Huang, J. Cao, T. Huang, R. Li, Q. Zhang, S. C. Lee and W. Ho, *J. Hazard. Mater.*, 2022, **424**, 127217.

47 L. Buzzetti, G. E. M. Crisenza and P. Melchiorre, *Angew. Chem., Int. Ed.*, 2019, **58**, 3730–3747.

48 Z. Cai, J. Zhong, J. Li and H. Jin, *Inorg. Chem. Commun.*, 2021, 126.

49 S. Zhong, B. Wang, H. Zhou, C. Li, X. Peng and S. Zhang, *J. Alloys Compd.*, 2019, **806**, 401–409.

50 Y. Geng, N. Li, J. Ma and Z. Sun, *J. Energy Chem.*, 2017, **26**, 416–421.

51 C. Yan, Z. Zhang, W. Wang, T. Ju, H. She and Q. Wang, *J. Mater. Sci.: Mater. Electron.*, 2018, **29**, 18343–18351.

52 W. Zeng, L. Feng, Y. Yu, J. Wang and Z. Liu, *J. Alloys Compd.*, 2021, 850.

53 J. Wiktor, F. Ambrosio and A. Pasquarello, *ACS Energy Lett.*, 2018, **3**, 1693–1697.

54 S. Ashwini, S. C. Prashantha, R. Naik, Y. V. Naik, H. Nagabhushana and K. N. Narasimhamurthy, *J. Sci.: Adv. Mater. Devices*, 2019, **4**, 531–537.

55 X. Wang, L. Liu, H. An, Y. Zhong, D. Wang, C. Tang and C. Hu, *Mater. Res. Bull.*, 2019, **118**.